

## Yielding under compression and the polyamorphic transition in silicon

Jan Griebner<sup>1</sup>, Gianpietro Moras<sup>2</sup>, and Lars Pastewka<sup>1,3,\*</sup>

<sup>1</sup>Department of Microsystems Engineering, University of Freiburg, Georges-Köhler-Allee 103, 79110 Freiburg, Germany

<sup>2</sup>Fraunhofer IWM, MikroTribologie Centrum  $\mu$ TC, Wöhlerstraße 11, 79108 Freiburg, Germany

<sup>3</sup>Cluster of Excellence livMatS, Freiburg Center for Interactive Materials and Bioinspired Technologies, University of Freiburg, 79110 Freiburg, Germany



(Received 24 February 2023; revised 11 May 2023; accepted 15 May 2023; published 30 May 2023)

We investigate the behavior of amorphous silicon under hydrostatic compression using molecular simulations. During compression, amorphous silicon undergoes a transformation from a low-density to a high-density structure. Depending on the temperature and the compression rate, the transformation occurs in a pressure range between 6 and 16 GPa. Ensemble-averaged density and elastic constants change discontinuously across the transition. Densification of individual glassy samples occurs through a series of discrete plastic events, each of which is accompanied by a vanishing shear modulus. This is the signature of a series of elastic instabilities, similar to shear transformation zones observed during shear yielding of glasses. We compare the structure obtained during compression with a quasiequilibrium form of amorphous silicon obtained by quenching a melt at constant pressure. This gives structures identical to compression at low and high pressure, but the transition between low- and high-pressure structures occurs gradually rather than discontinuously. Our observations indicate that the polyamorphic transition has the characteristics of a yield transition that occurs under compression instead of shear.

DOI: [10.1103/PhysRevMaterials.7.055601](https://doi.org/10.1103/PhysRevMaterials.7.055601)

### I. INTRODUCTION

Materials can exist in structurally distinct forms in their crystalline state, a property which is called *polymorphism* [1]. Which form is actually present depends on the external conditions of temperature and pressure and on the way the material is formed and processed afterwards. One form can transform into another, for example, when increasing the pressure above some critical value. In crystals, pressure-induced phase transitions are commonly between equilibrium states of the system [2–4]. Amorphous solids, however, are intrinsically out-of-equilibrium, yet pressure-induced transformations between distinct amorphous forms are possible [5–10].

Materials with multiple amorphous modifications are called *polyamorphic* [5–8,10]. One prominent example of a material featuring such a polyamorphic phase transition is silicon [11–19]. Silicon crystallizes into the diamond cubic phase under ambient conditions and transforms into the  $\beta$ -Sn phase upon hydrostatic compression [20]. An indication for a polyamorphic transition in the corresponding amorphous form is that the melting temperature  $T^m$  in silicon decreases with increasing pressure,  $dT^m/dP < 0$  [see Fig. 1(a)], meaning that the liquid phase is denser than the low-temperature diamond cubic crystal. A maximum in the melting curve, which for silicon is expected to occur at negative pressure

[7,21–23], is typically explained by a “two-state” model [24]. This model assumes that low-density and high-density phases coexist in the liquid state, with the proportion of high-density domains increasing with pressure, thus leading to a pressure-driven transition from a low-density to a high-density liquid phase [7,10,13,22,25–28]. A transition between two amorphous modifications is expected to reflect this liquid-liquid phase transition.

Experimental studies have revealed that amorphous silicon (aSi) can indeed exist in two distinct structures. Upon compression, aSi transforms from a low-density structure (LDA) to a high-density structure (HDA) at a critical pressure between  $P^c \approx 12$  and 16 GPa [11,15,29,30]. A further increase in hydrostatic pressure results in recrystallization, indicating that the HDA phase is metastable [16,20]. These experiments were supported by early numerical simulations, which showed a transition from an initially fourfold-coordinated LDA structure to an HDA structure with fivefold-coordinated atoms [14], or to a very-high-density amorphous (VHDA) structure with even higher coordination [12]. This structural transformation of aSi has been numerically investigated by multiple authors since, always showing a coexistence of LDA and HDA regions that sequentially transform to HDA (or VHDA) during compression [12,14,18,19]. Molecular simulations have recently also been shown to yield recrystallization of the HDA phase [19].

There are multiple well-documented mechanisms that lead to structural transitions between polymorphs. Besides equilibrium phase transitions, crystalline materials have ultimate stability limits where the crystalline lattice collapses as a consequence of an elastic or dynamic instability [31–34]. The result of such an instability is that all atoms in a

\*Corresponding author: [lars.pastewka@imtek.uni-freiburg.de](mailto:lars.pastewka@imtek.uni-freiburg.de)

Published by the American Physical Society under the terms of the [Creative Commons Attribution 4.0 International](https://creativecommons.org/licenses/by/4.0/) license. Further distribution of this work must maintain attribution to the author(s) and the published article's title, journal citation, and DOI.

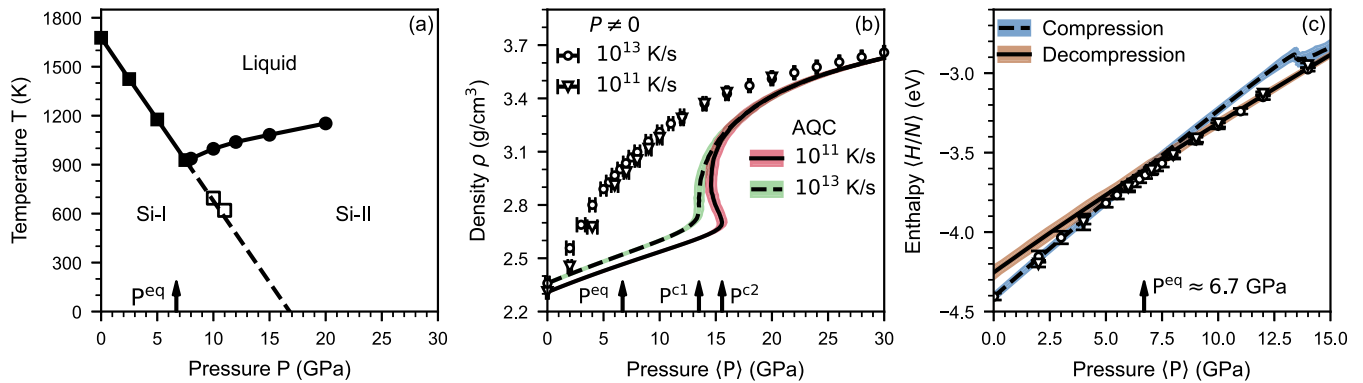


FIG. 1. (a) Pressure-temperature phase diagram of silicon obtained from atomistic simulations via phase-coexistence calculations. (Data are from Ref. [18].) Si-I is the diamond cubic and Si-II is the  $\beta$ -Sn phase of silicon. (b) Density of amorphous silicon as a function of hydrostatic pressure. The dashed and solid lines are glasses hydrostatically compressed in AQC simulations and initially prepared at vanishing pressure. Dots and triangles represent glasses quenched from the liquid while maintaining the constant nonzero hydrostatic pressure. Lines and open symbols indicate the ensemble mean while shaded areas and error bars mark the standard deviation. The vertical arrow  $P^{eq}$  marks the critical pressure for the expected equilibrium transformation (see panel c for its definition),  $P^{c1} = 13.5$  GPa and  $P^{c2} = 15.6$  GPa mark the critical pressures for the mechanical transformation. (c) Enthalpy during AQC simulations of compression and subsequent decompression of an ensemble of glasses prepared with a quench rate of  $\dot{T} = 10^{13}$  K/s. The vertical arrow  $P^{eq} \approx 6.7$  GPa marks the intersection of the enthalpy curves during compression and decompression.

perfect and defect-free crystal rearrange at once, forming a new stable crystal. Plasticity during shear loading of amorphous structures is associated with similar, yet localized mechanical instabilities [35–40]. The rearranging regions are called shear-transformation zones and their occurrence can be predicted through the identification of “soft spots” [39–42]. In aSi, these soft spots are local regions of HDA character [43,44]. This raises the question of whether plasticity in amorphous solids and the polyamorphic transition have different microscopic signatures or, conversely, whether this transition is nothing more than some sort of yield point.

In the theory of equilibrium phase transitions, the distinction between first and second order is made on the behavior of susceptibilities across the transition point [4,45]. A partial answer to the question on the nature of the polyamorphic transition may therefore rest in how the (linear) mechanical response of aSi behaves across the transition. We here use atomic-scale computer simulations of periodic representative amorphous volume elements to study the macroscopic (elastic) and microscopic (shear transformation) response of aSi across the polyamorphic transition. To drive the transition, we compress (and decompress) these volume elements affinely in small increments, and we search for the next local minimum after the deformation step. We call this procedure athermal quasistatic *compression* (AQC), in analogy to the athermal quasistatic *shear* procedure used in the amorphous plasticity literature [46,47]. It mimics experiments where pressure is induced either through a pressure medium in a loading cell or by contacting with an indenter [11,15,16,20,29,30].

Our results indicate that the collapse of the aSi structure has signatures similar to the yield point during shear loading. The transition can be viewed as a sequential series of spatially localized compression transformation zones or plastic events. To emphasize the mechanical character of the transition, we also probe the properties of a form of aSi that is compressed

in the liquid phase and then quenched at constant pressure to become amorphous. The resulting amorphous samples show a gradual, rather than a discontinuous, variation of thermodynamic properties (density, elastic constants) as a function of pressure.

## II. METHODS

We employ molecular dynamics and molecular statics simulations to investigate the behavior of aSi under hydrostatic compression. We first melt a Si-I (diamond cubic) crystal with  $N = 4096$  atoms in the isothermal-isobaric (NPT) ensemble at  $T = 3000$  K and zero hydrostatic pressure. The liquid is cooled down to  $T = 2000$  K at a constant rate of  $\dot{T} = 10^{13}$  K/s and equilibrated for a further 20 ps.

Our final aSi configurations are prepared from this silicon melt in three distinct ways. First, we produce periodic representative volume elements of aSi at zero hydrostatic pressure. We draw new random velocities from a Gaussian distribution at  $T = 2000$  K and equilibrate the structures for 30 ps. This equilibration time is sufficient for the atoms to lose the memory of their initial state, i.e., for the mean-squared displacement to be in the diffusive regime. After equilibration, we quench the liquid samples from  $T = 2000$  K to  $T = 1$  K at quench rates of  $\dot{T} = 10^{13}$  K/s and  $\dot{T} = 10^{11}$  K/s. To drive the polyamorphic transition, the final glass is then compressed hydrostatically by affinely remapping all atomic positions with a prescribed density increment  $\Delta\rho$  [46,47]. We optimize the glass structure after each increment, a procedure we refer to as AQC in the following.

Second, we reheat the final aSi structure from  $T = 1$  K to a finite temperature of  $T \leq 700$  K which is smaller than the glass transition temperature  $T_G \approx 1100$  K. The glasses are equilibrated for 200 ps at temperature  $T$  and vanishing hydrostatic pressure  $P$ . After equilibration, these configurations are compressed hydrostatically at constant

temperature and compression rates of  $\dot{P} = 10^{-4}$  GPa/ps and  $\dot{P} = 10^{-5}$  GPa/ps.

Third, we equilibrate the liquid silicon at  $T = 2000$  K and a set of constant hydrostatic pressures of  $P \neq 0$  GPa. The liquid is quenched to  $T = 1$  K using quench rates of  $\dot{T} = 10^{13}$  K/s and  $\dot{T} = 10^{11}$  K/s while maintaining constant hydrostatic pressure. We generate ensembles of 500 independent configurations for the glasses quenched at vanishing pressure and the subsequent AQC. Compression at finite temperature is performed for a subset of 10 configurations. For the glasses prepared at nonzero hydrostatic pressure, we generate 100 configurations for  $\dot{T} = 10^{13}$  K/s and 25 configurations for  $\dot{T} = 10^{11}$  K/s at each pressure.

In all simulations, we used the interatomic potential by Kumagai *et al.* [48]. Previous publications showed that this interatomic potential correctly reproduces the polymorphic transition in aSi [18] and delivers results on shear-induced silicon amorphization that are comparable to those obtained with more complex machine-learning potentials [49–51]. All dynamic simulations employed a timestep  $\Delta t = 1$  fs, a Nose-Hoover chain thermostat, and a Parrinello-Rahman barostat [52–54]. The relaxation constant of the thermostat and the barostat were chosen as 1 and 10 ps, respectively. Energy minimization in static simulations was performed using a conjugate-gradient minimizer with a force tolerance of  $10^{-6}$  eV/Å.

### III. RESULTS

#### A. Phenomenology

We begin by investigating how amorphous silicon prepared at zero pressure behaves under hydrostatic compression. As shown in Fig. 1(b), the density initially increases linearly with pressure. The material densifies at constant critical pressure  $P^c$ , which manifests as an abrupt increase in the density-pressure diagram. This sudden compression is the signature of the pressure-driven transformation from an LDA to an HDA structure in aSi. The critical pressures for this transition are at  $P^{c1} \approx 13.5$  GPa and  $P^{c2} \approx 15.6$  GPa for glasses prepared with quench rates of  $10^{13}$  and  $10^{11}$  K/s, respectively. As the system is further compressed, the mean density of glasses prepared with different quench rates converges to the same value. The glasses prepared at a constant nonzero pressure show a smooth dependence on the hydrostatic pressure and therefore a continuous transition between the two phases. These results are consistent with prior work [18,19].

Additional insight can be obtained by comparing the enthalpy  $H$  of the two phases [3,12,55],  $H = U + PV$ , where  $U$  is the potential energy,  $P$  is the pressure, and  $V$  is the volume. In Fig. 1(c), we show the enthalpy during compression and subsequent decompression. The two curves intersect at  $P^{eq} \approx 6.7$  GPa, which is the pressure at which a quasiequilibrium phase transformation could occur. Here quasiequilibrium has to be interpreted as a transition between two metastable basins in the potential energy landscape; i.e., at finite temperature we would need to restrict phase-space integrals to the respective basin to avoid jumps between them. We observe that glasses prepared at constant pressure follow the amorphous structure with the lowest enthalpy. We conclude that below 6.7 GPa the

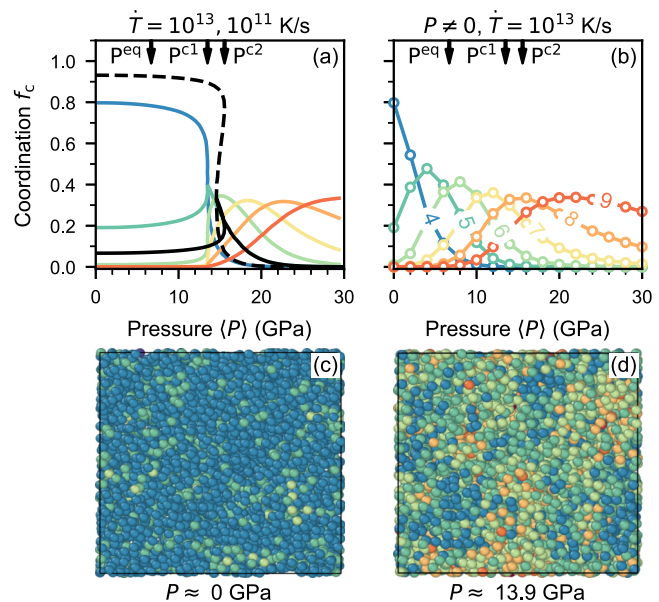


FIG. 2. [(a), (b)] Probability  $f_c$  of finding an atom with coordination  $c$  as a function of hydrostatic pressure for glasses prepared at zero pressure (a) and at constant nonzero pressure (b) from ensembles of simulation runs. Colored lines mark samples prepared initially with a quench rate of  $\dot{T} = 10^{13}$  K/s. The black dashed line shows  $f_4$  and the black solid line shows  $f_5$  for glasses prepared with a quench rate of  $\dot{T} = 10^{11}$  K/s. We only show  $f_4$  and  $f_5$  for the latter since atoms with higher coordination behave similarly for compression larger than the critical pressure. The spatial cutoff for the computation of the coordination number is chosen as  $r_c = 2.925$  Å as obtained from the first local minimum in the radial distribution function at zero pressure. The vertical arrows indicate  $P^{eq}$ ,  $P^{c1}$ , and  $P^{c2}$  as in Fig. 1. [(c), (d)] Visualization of the coordination number  $c$  for an exemplary atomic configuration quenched with  $\dot{T} = 10^{13}$  K/s in the LDA structure (c) and in the HDA structure (d). Color coding is the same as that in panels (a) and (b).

LDA structure is thermodynamically preferred, while above 6.7 GPa the HDA structure is more favorable. The critical pressures  $P^c$  obtained from compression are more than twice this quasiequilibrium pressure  $P^{eq}$ .

We now analyze how the atomic structure changes across this transition. Figures 2(a) and 2(b) show the probability  $f_c$  of finding an atom with coordination  $c$ . For glasses prepared at a quench rate of  $10^{13}$  K/s we show  $c \in \{4, \dots, 9\}$ , while we only show  $c \in \{4, 5\}$  for the slower quench rate of  $10^{11}$  K/s. During hydrostatic compression, before  $P^c$  is reached, we observe only small changes in the mean coordination  $\sum_c c f_c$ . In this regime, slowly quenched glasses have a larger fraction  $f_4$  of fourfold-coordinated atoms than samples prepared with a fast quench rate. Upon reaching the critical pressure,  $f_4$  drops and an atomic configuration with mainly fivefold-coordinated atoms (large  $f_5$ ) emerges. These fivefold-coordinated configurations are transient and vanish rapidly as atoms with even higher coordination numbers 6, 7, 8, and 9 emerge continuously for increasing hydrostatic pressure. The snapshots of compressed configurations in Figs. 2(c) (LDA) and 2(d) (HDA) also clearly show this increase in average coordination across the LDA-HDA transition. Note that some

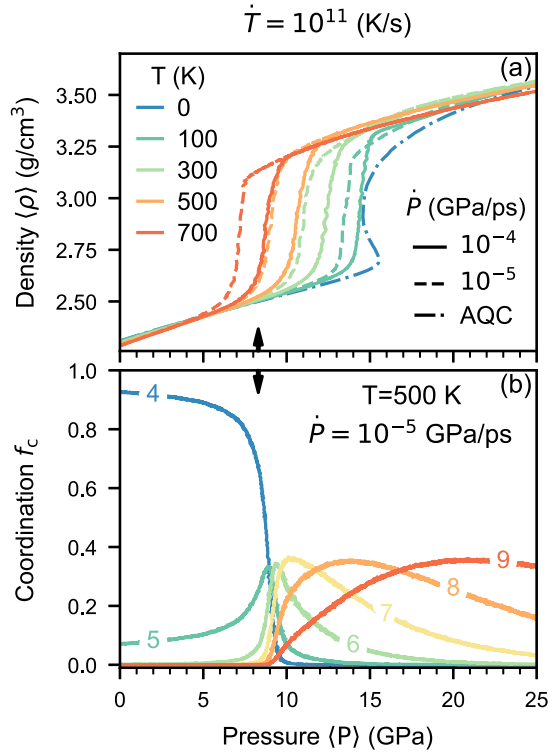


FIG. 3. (a) Ensemble-averaged density  $\langle \rho \rangle$  of aSi as a function of hydrostatic pressure  $P$  at finite temperature and compression rate. (b) Probability  $f_c$  for one atom with coordination  $c$  as a function of hydrostatic pressure. The black arrows indicate approximately the critical pressure for the transformation from LDA to HDA for configurations compressed with  $\dot{P} = 10^{-5}$  GPa/ps at  $T = 500$  K.

authors denote structures with high-coordination numbers as VHDA [12,14,19,56], but given the gradual transition towards highly coordinated structures we refer to the high-pressure structures as HDA. For glasses quenched at a constant pressure, the coordination number changes continuously with hydrostatic pressure. Thereby, low-coordinated atoms are continuously replaced by atoms with higher coordination as the pressure increases. At the pressure  $P^{c\text{q}} = 6.7$  GPa, the configurations consist mainly of five- and sixfold-coordinated atoms.

So far we have considered mechanical compression in the athermal limit, i.e., at vanishing temperature [46,47]. In Fig. 3(a), we show the mean density of aSi during hydrostatic compression at finite temperature. For each investigated temperature and compression rate we observe a critical pressure  $P^c$  at which the density increases abruptly, indicating an LDA-HDA transformation. This critical pressure decreases with increasing temperature  $T$  and decreasing compression rate  $\dot{P}$ . Compared to the athermal limit, the minimal critical pressure for the highest temperature  $T = 700$  K and the slowest compression rate  $\dot{P} = 10^{-5}$  GPa/ps is reduced to  $\approx 39\%$ .

Similar to Figs. 2(a) and 2(b), we show in Fig. 3(b) the pressure-dependent coordination for one exemplary temperature and compression rate. The initial coordination changes drastically at the critical pressure. In contrast to the athermal simulations, the transition is smooth and we observe more changes in coordination at pressures below

the zero-temperature critical pressure; however, the overall phenomenology is identical. Since the signature of the polyamorphous transformation is best observed at zero temperature, we only consider the athermal simulations for the rest of the paper.

## B. Elastic properties

The abrupt change in coordination during athermal compression, as opposed to a continuous pressure dependency, is reminiscent of a first-order phase transition. To further substantiate this analogy, we investigate the relevant susceptibilities, i.e., the elastic constants, across the polyamorphous transition. It is well known that in crystalline materials a mechanically driven transition occurs when an eigenvalue of the elastic tensor  $C_{\alpha\beta\mu\nu}$  disappears [32,57,58]. In the limit of zero temperature and finite stress, the tensor of elastic moduli  $C_{\alpha\beta\mu\nu}$  (also known as the Birch coefficients [33,34,59,60]) is composed of three contributions: the affine or Born moduli  $C_{\alpha\beta\mu\nu}^B$ , the nonaffine moduli  $C_{\alpha\beta\mu\nu}^{\text{NA}}$ , and a stress-dependent contribution  $C_{\alpha\beta\mu\nu}^S$ . The full elastic tensor is computed as [34,61–63]

$$C_{\alpha\beta\mu\nu} = C_{\alpha\beta\mu\nu}^B + C_{\alpha\beta\mu\nu}^{\text{NA}} + C_{\alpha\beta\mu\nu}^S, \quad (1)$$

with

$$C_{\alpha\beta\mu\nu}^B = \frac{1}{V} \frac{\partial^2 U(r_{ij})}{\partial \eta_{\alpha\beta} \partial \eta_{\mu\nu}}, \quad (2)$$

$$C_{\alpha\beta\mu\nu}^{\text{NA}} = -\frac{1}{V} \frac{\partial^2 U(r_{ij})}{\partial r_{i\gamma} \partial \eta_{\alpha\beta}} (\mathcal{H}^{-1})_{l\gamma, m\kappa} \frac{\partial^2 U(r_{ij})}{\partial r_{m\kappa} \partial \eta_{\mu\nu}}, \quad (3)$$

$$C_{\alpha\beta\mu\nu}^S = \frac{1}{2} (\sigma_{\alpha\mu} \delta_{\beta\nu} + \sigma_{\alpha\nu} \delta_{\beta\mu} + \sigma_{\beta\mu} \delta_{\alpha\nu} + \sigma_{\beta\nu} \delta_{\alpha\mu} - 2\sigma_{\alpha\beta} \delta_{\mu\nu}), \quad (4)$$

where  $U(r_{ij})$  is the energy function,  $V$  is the current volume of the simulation cell,  $r_{i\gamma}$  is the position of atom  $i$  in direction  $\gamma$ ,  $\eta_{\alpha\beta}$  is the Green-Lagrange strain tensor,  $\sigma_{\alpha\beta}$  is the Cauchy stress,  $\delta_{\alpha\beta}$  is the Kronecker delta and  $\mathcal{H} = \partial^2 U(r_{ij}) / \partial r_{l\phi} \partial r_{m\psi}$  is the Hessian matrix. More details on this decomposition at finite stress and its analytical computation for many-body potentials can be found in Ref. [34].

Since amorphous solids show isotropic material behavior for sufficiently large system sizes and we consider a hydrostatic stress, the elastic tensor  $C_{\alpha\beta\mu\nu}$  reduces to two independent elastic constants [61,64–66]. We report the ensemble-averaged bulk modulus  $K$  and shear modulus  $\mu$ , since they are the eigenvalues of the elastic tensor. They determine the limit of elastic stability that is reached when either modulus vanishes [31,32]. Only the shear modulus can vanish under hydrostatic compression.

Figure 4 shows the bulk modulus  $K$  and the shear modulus  $\mu$  for the full range of pressures. The bulk modulus of the glasses increases under compression for the full pressure range, independent of preparation. For aSi prepared at vanishing pressure, the bulk modulus initially increases linearly up to  $P \approx 8$  GPa and starts to become independent of pressure up to  $P^c$ . During the transformation (at  $P^c$ ), the bulk modulus increases discontinuously and subsequently approaches again a linear pressure dependency for higher compression. For glasses prepared at constant, nonzero pressure we observe a

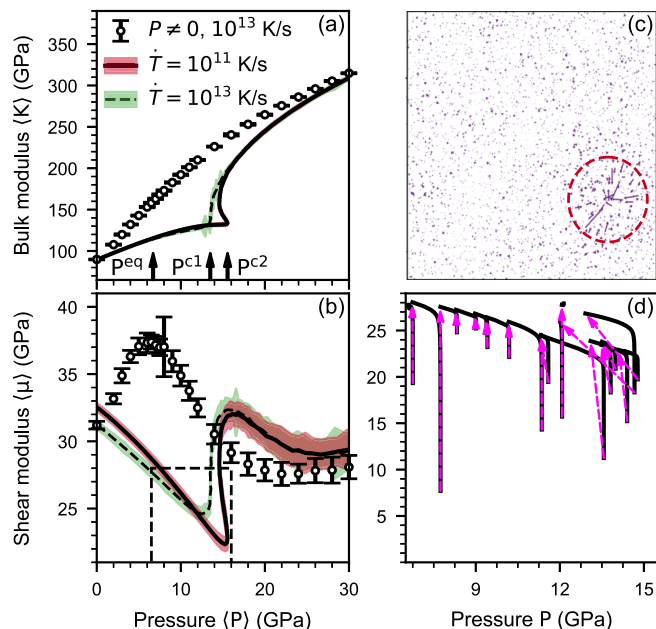


FIG. 4. Pressure-dependent ensemble-averaged (a) bulk modulus  $\langle K \rangle$  and (b) shear modulus  $\langle \mu \rangle$  (c) Exemplary nonaffine displacement field resulting from one elastic instability. Note that the displacement vectors are scaled with a constant value  $x$  for better visibility and the red circle is a guide to the eye and marks the location of largest displacement. (d) Pressure-dependent shear modulus  $\mu$  of the black dashed box in panel (b) for one single configuration prepared using  $\dot{T} = 10^{11}$  K/s. The pink dashed arrows indicate the jumps in pressure and shear modulus during each instability.

continuous, but sublinear, increase of the bulk modulus with increasing pressure. The pressure dependency of the bulk modulus resembles the pressure dependency of the density in Fig. 1(b). The difference between the quenched and AQC glasses is purely due to their difference in density. The bulk modulus data collapse when plotted versus density rather than pressure.

The shear modulus  $\mu$  shows more interesting features. During AQC, the shear modulus  $\mu$  decreases to a value of about 24 GPa at the critical pressure. Once  $P^c$  is reached, the modulus jumps to a value of roughly 32 GPa, almost identical to the modulus for the stress-free quenched structure. While the initial quench rate leads to a different modulus at  $P < P^c$ , the systems appear to lose memory of the initial state beyond the polyamorphic transformation. At even larger compression, the shear modulus starts to soften again. The shear modulus is independent of the preparation protocol above the critical pressure of the polyamorphic transition.

For glasses quenched at constant pressure, the shear modulus also has a nonmonotonic functional dependency on  $P$ . The maximum shear modulus is at  $P \approx 6.8$  GPa, which coincides with the critical pressure  $P^{eq}$  of the quasiequilibrium transformation. As the pressure increases above  $P^{eq}$  and  $P^c$ , the shear modulus decreases and plateaus at  $P \gtrsim 20$  GPa.

In Fig. 5 we show the individual contributions from Eq. (1) to the bulk modulus and the shear modulus. For AQC aSi, the pressure dependency of the Born contribution to the bulk modulus is qualitatively similar to what is observed for the

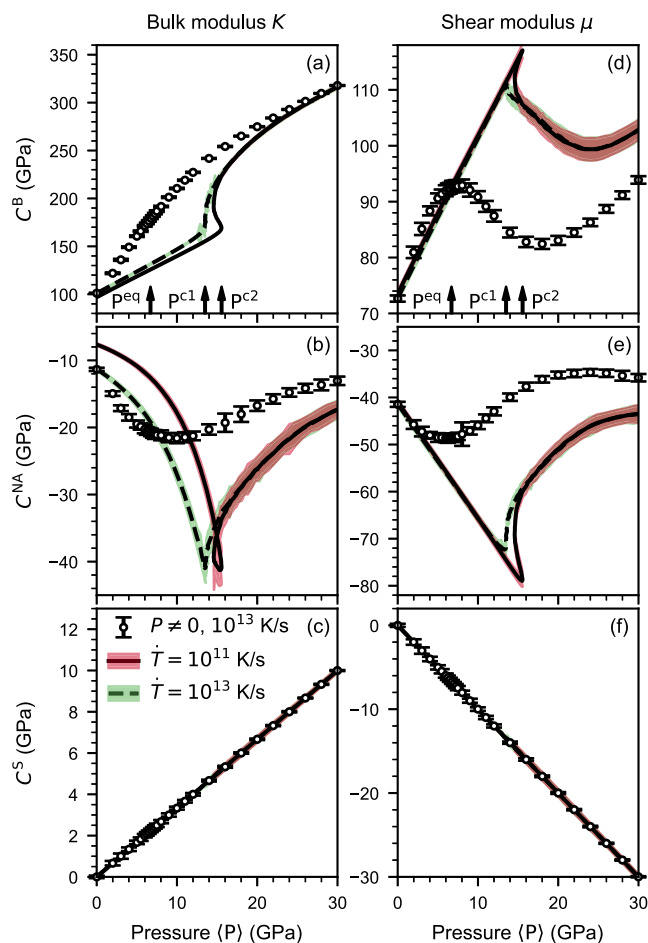


FIG. 5. Born  $C^B$ , stress  $C^S$ , and nonaffine  $C^{NA}$  contributions of the bulk modulus  $\langle K \rangle$  [panels (a)–(c)] and the shear modulus  $\langle \mu \rangle$  [panels (d)–(f)].

full bulk modulus in Fig. 4(a). While the Born contribution hardens the elastic response, the nonaffine contribution softens it. With increasing compression, the magnitude of the nonaffine contribution increases initially and reaches a local maximum at the critical pressure. At the critical pressure, the ratio between the Born and the nonaffine contribution has a local minimum of  $C^B/|C^{NA}| \approx 4$ . This minimum explains the flattening of the bulk modulus observed in Fig. 4(a). Above the transformation, the nonaffine contribution decreases its magnitude with pressure. The aSi samples prepared at a constant pressure show a pressure dependency similar to the AQC glasses for both the Born and the nonaffine contribution. However, their pressure dependency is continuous and no abrupt change of either property is observed. As expected from Eq. (4), the stress contribution increases linearly and is independent of the preparation protocol. The stress contribution additionally stiffens the material, but its absolute value is small compared to the Born contribution.

The Born contribution to the shear modulus increases linearly under hydrostatic compression for the aSi samples prepared at vanishing pressure. The behavior of the nonaffine contribution is the reverse of the Born contribution; i.e., the magnitude of the nonaffine contribution decreases linearly. At the critical pressure for the transformation, the two

contributions have a local maximum, or respectively minimum, with a ratio of  $C^B/|C^{NA}| \approx 1.4$ : The nonaffine contribution almost compensates the Born term. At the transformation, the pressure dependency changes abruptly. For larger compression, the affine contribution decreases and the nonaffine contribution increases. The stress-dependent part of the shear modulus softens the elastic response in addition to the nonaffine contribution. This ultimately explains the observed softening of the shear modulus in Fig. 4 before the transformation. Samples prepared at constant pressure follow again the trends of the hydrostatically compressed glasses but without the abrupt change in behavior.

### C. Elastic instabilities and soft spots

Although the (ensemble-averaged) shear modulus softens under compression, its value at the critical pressure for the phase transformation is still finite. The material does not appear to exhibit an elastic instability. While the ensemble-averaged data do not show an instability, the individual calculations undergo a continuous series of elastic instabilities, i.e., a divergence of the shear modulus in the pressure range of the polyamorphous transition. Figure 4(c) shows the nonaffine displacement field resulting from one of these elastic instabilities. This nonaffine displacement field reveals a random displacement of all atoms, but localized on one cluster of atoms. Figure 4(d) shows the drops in the shear modulus resulting from a sequence of such events. Comparing the shear modulus before and after an instability, we observe that the absolute value barely changes for pressures  $P < P^c$ . At the critical pressure  $P^c$  for the transformation (which is slightly configuration dependent), the number of elastic instabilities per pressure range increases. Interestingly, each instability near  $P^c$  leads to a noticeable stiffening of the shear modulus.

We investigate the origin of this sudden change by looking at the microscopic signature of these individual plastic events, which are reminiscent of shear transformation zones (STZs) but occur under compression rather than shear. Many methods exist to predict and identify soft spots in amorphous solids [40]. In this work we use the method developed by Richard *et al.* [67], which relies on the pseudoharmonic modes (PHMs). We choose PHMs because they predict the displacement field of a soft spot well before the instability [67]. We compute the lowest PHM for a subset of 50 configurations as a function of hydrostatic pressure and report their approximate size using the participation ratio. The participation ratio  $e$  is defined as

$$Ne = \left[ \sum_i (\bar{\pi}_i \cdot \bar{\pi}_i)^2 \right]^{-1}, \quad (5)$$

where  $\pi$  (which is a  $3N$ -dimensional vector) is the displacement field of the PHM and  $N$  is the number of atoms in the solid. The participation ratio  $e$  is a measure of spatial localization and  $Ne$  is the approximate number of atoms participating in the plastic event. For the special case where only one atom is involved in a plastic event, it yields  $Ne = 1$ . In contrast, if all atoms are involved and they contribute equally,  $Ne = N$ .

Figures 6(a) and 6(b) show the product  $Ne$  of the PHM as a function of hydrostatic pressure. The mean size of the

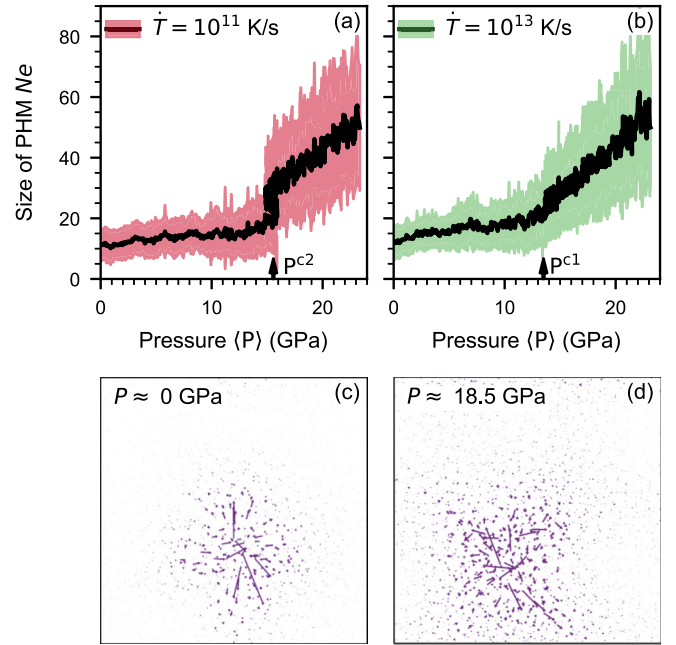


FIG. 6. [(a), (b)] Pressure dependence of the number of atoms contributing in one pseudoharmonic mode (PHM). The black vertical arrows mark the critical pressures  $P^c$  from Fig. 1(b). [(c), (d)] Displacement fields  $\bar{\pi}_i$  for PHMs for one sample prepared at  $\dot{T} = 10^{13}$  K/s.

PHMs increases slightly with compression before the phase transformation. Independent of quench rate, the mean size of the PHMs in this regime involves approximately 10–20 atoms. At the transformation pressure, the mean size of the soft spots starts to increase up to  $\approx 30$  atoms. For larger compression, the number of atoms involved in a plastic event increases up to approximately 50 atoms. The displacement field  $\pi$  for one of the modes in the low- and high-pressure regimes is shown in Figs. 6(c) and 6(d). It is clearly visible that the size of the soft spots increases with compression and that the displacement field has an Eshelby-like character [40,68,69].

## IV. DISCUSSION

First, we note that equilibrium arguments appear to be incapable of capturing the polyamorphic transformation in aSi. In particular, the polyamorphic transformation does not occur near the “equilibrium” pressure  $P^{eq}$ . This transition is between different polymorphs of the aSi phase, which are not equilibrium configurations. Therefore, care has to be taken when interpreting this quasiequilibrium transformation.

$P^{eq}$  does capture aspects of the transition from low- to high-density structures when compressing the melt before quenching—in particular, the maximum in shear modulus [Fig. 4(b)]. This indicates a large kinetic barrier resisting the structural transition. The origin of this kinetic barrier is a low atomic mobility below  $T^G$ , which constrains the LDA structure to a region of metastability in the phase space. Poole *et al.* [70] employed a thermodynamic description and associated the actual critical pressure for the transformation with the limit of metastability, i.e., with a spinodal. Thereby, the spinodal marks the limit where any

thermodynamic barrier vanishes. However, an amorphous solid should be described by a multitude of spinodal lines or points, rather than a single one, owing to the random distribution of properties [71–73].

We observe that the density  $\rho$  of the configurations quenched at nonzero pressure is higher than the AQC compressed samples, but both yield a similar mean enthalpy  $H$ . This observation can be explained via the “two-state model” of Rapoport [8,10,24]. This model assumes that the liquid exists in two different states that in the case of aSi correspond to the Si-I (diamond cubic) and Si-II ( $\beta$ -tin) crystal phases. Because of the high mobility of the atoms in the liquid, the different states can be continuously created and annihilated, whereby their fraction can increase continuously under compression. Therefore, glasses equilibrated in the liquid at nonzero pressure can adjust their coordination which is frozen after quenching. The difference in density between the two ways of preparation is balanced by their energy difference. This is direct evidence that multiple polyamorphs exist in our simulations.

Our observations on the polyamorphic transition have similarities to shear yielding of glasses. Shear yielding of aSi has been reported in the literature, with the following phenomenology: aSi initially deforms elastically but flows after the yield point [44,69,74–76]; approaching the yield point, a large percentage of atoms become fivefold coordinated [44,74,75]; the shear modulus changes abruptly at the yield point [69]. We observed the same phenomena for the polyamorphic transition, with the difference that atoms with coordination larger than 5 appear during compression.

The microscopic picture of the polyamorphic transformation found here is also identical to yielding under shear in glasses. Hydrostatic compression of aSi results in a series of instabilities, which can be identified by a loss of mechanical stability that manifests as a vanishing shear modulus. Each instability triggers a soft spot in the material: The displacement field during these instabilities shows signatures identical to STZs [37,40,64], the carrier of plastic deformation in disordered materials under shear. These signatures include a localization of the nonaffine displacement field [41] as well as a quadrupolar strain-field surrounding the localized event, as described by Eshelby inclusion theory [68]. The fast-quenched configurations initially have a fraction of fivefold and higher-coordinated atoms larger than that of the configurations obtained at lower quench rates. These are “liquidlike”, i.e., less resistant to deformation and acting as soft spots in aSi [43,44]. This lower resistance to deformation reduces the critical pressure.

The macroscopic shear modulus, computed here as ensemble averages over 500 configurations, does not vanish. However, it monotonously decreases with pressure below  $P^c$  of the polyamorphic transformation and jumps to a larger value as the transition is crossed. This is accompanied by an instantaneous change in density, marked by an increase in average coordination. The decrease in shear modulus is driven by the nonaffine contribution to the elastic modulus [Fig. 5(e)]. In terms of the microscopic picture painted in the previous paragraph, the nonaffine origin of the decrease in shear modulus can be interpreted as a signature of localized softening of the material.

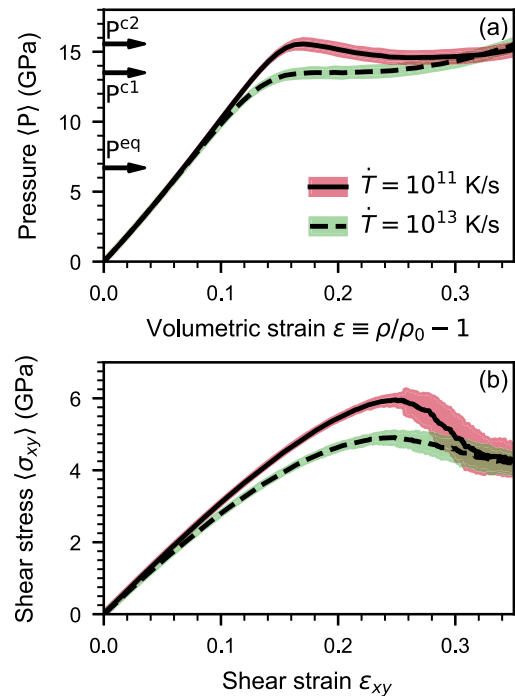


FIG. 7. (a) Hydrostatic pressure as a function of volumetric strain  $\varepsilon$ . The volumetric strain is computed as  $\varepsilon = \rho/\rho_0 - 1$ , where  $\rho_0$  is the initial density. (b) Shear stress as a function of shear strain.

To further emphasize the similarities to yielding, we plot in Fig. 7(a) the pressure as a function of volumetric strain in a traditional stress-strain diagram. The behavior is qualitatively identical to stress-strain diagrams obtained from shear yielding glasses [43,44,47,74,75,77], with pressure taking the role of shear stress. For visual comparison, we also computed the shear response of our aSi samples and show in Fig. 7(b) the ensemble-averaged shear stress  $\sigma_{xy}$  as a function of the shear strain  $\varepsilon_{xy}$ . The material exhibits a linear “elastic” response at small strain  $\varepsilon$  followed by flow at constant pressure beyond a yield point at  $\varepsilon \gtrsim 0.1$  and both compression and shear. In particular, the glass prepared at a lower quench rate shows a stress overshoot, explaining the re-entrant section of the density-pressure diagram [Fig. 1(b)] as a compression-softening phenomenon of a well-aged glass [44,77,78].

## V. CONCLUSIONS

In summary, we performed extensive simulations of the behavior of aSi during hydrostatic compression. Our simulations show a polyamorphic transformation from a low-density to a high-density phase during quasistatic compression of aSi quenched at zero pressure, but a gradual transition for near-equilibrium structures obtained when quenching liquid silicon at a finite pressure. Microscopic and macroscopic analyses of the transition revealed similarities to the yield transition of glasses under shear: localized carriers of plastic events (shear transformation zones), change of local atomic order, and change in elastic properties. We conclude that the polyamorphic transition is essentially a yield transition. Whether yield of glasses itself is a phase transition is an open discussion in the scientific literature [77,79–82].

## ACKNOWLEDGMENTS

We thank Richard Leute and Thomas Reichenbach for fruitful discussions. Molecular dynamics simulations were carried out with LAMMPS [83,84]. We used ASE [85] and MATSCIPY [86] for analysis of results and computation of

the elastic properties. Atomic configurations were visualized with OVITO [87]. The authors acknowledge support from the Deutsche Forschungsgemeinschaft (DFG, Grant No. PA 2023/2). Simulations were carried out on NEMO at the University of Freiburg (DFG Grant No. INST 39/963-1 FUGG).

- [1] W. D. Callister and D. G. Rethwisch, *Materials Science and Engineering* (Wiley, New York, 2007), Vol. 7.
- [2] H. E. Stanley, *Phase Transitions and Critical Phenomena* (Clarendon, Oxford, 1971), Vol. 7.
- [3] R. Kubo, M. Toda, and N. Saito, *Statistical Physics I: Equilibrium Statistical Mechanics* (Springer, Berlin, 1998).
- [4] F. Schwabl, *Statistical Mechanics* (Springer, Berlin, 2006).
- [5] P. H. Poole, T. Grande, C. A. Angell, and P. F. McMillan, Polymorphic phase transitions in liquids and glasses, *Science* **275**, 322 (1997).
- [6] V. V. Brazhkin and A. G. Lyapin, High-pressure phase transformations in liquids and amorphous solids, *J. Phys.: Condens. Matter* **15**, 6059 (2003).
- [7] M. C. Wilding, M. Wilson, and P. F. McMillan, Structural studies and polymorphism in amorphous solids and liquids at high pressure, *Chem. Soc. Rev.* **35**, 964 (2006).
- [8] P. F. McMillan, M. Wilson, M. C. Wilding, D. Daisenberger, M. Mezouar, and G. N. Greaves, Polyamorphism and liquid-liquid phase transitions: Challenges for experiment and theory, *J. Phys.: Condens. Matter* **19**, 415101 (2007).
- [9] D. Machon, F. Meersman, M. C. Wilding, M. Wilson, and P. F. McMillan, Pressure-induced amorphization and polyamorphism: Inorganic and biochemical systems, *Prog. Mater. Sci.* **61**, 216 (2014).
- [10] H. Tanaka, Liquid-liquid transition and polyamorphism, *J. Chem. Phys.* **153**, 130901 (2020).
- [11] S. K. Deb, M. Wilding, M. Somayazulu, and P. F. McMillan, Pressure-induced amorphization and an amorphous-amorphous transition in densified porous silicon, *Nature (London)* **414**, 528 (2001).
- [12] M. Durandurdu and D. A. Drabold, *Ab initio* simulation of first-order amorphous-to-amorphous phase transition of silicon, *Phys. Rev. B* **64**, 014101 (2001).
- [13] S. Sastry and C. Austen Angell, Liquid-liquid phase transition in supercooled silicon, *Nat. Mater.* **2**, 739 (2003).
- [14] T. Morishita, High Density Amorphous Form and Polyamorphic Transformations of Silicon, *Phys. Rev. Lett.* **93**, 055503 (2004).
- [15] P. F. McMillan, M. Wilson, D. Daisenberger, and D. Machon, A density-driven phase transition between semiconducting and metallic polyamorphs of silicon, *Nat. Mater.* **4**, 680 (2005).
- [16] N. Garg, K. K. Pandey, K. V. Shanavas, C. A. Betty, and S. M. Sharma, Memory effect in low-density amorphous silicon under pressure, *Phys. Rev. B* **83**, 115202 (2011).
- [17] D. Daisenberger, T. Deschamps, B. Champagnon, M. Mezouar, R. Quesada Cabrera, M. Wilson, and P. F. McMillan, Polyamorphic amorphous silicon at high pressure: Raman and spatially resolved x-ray scattering and molecular dynamics studies, *J. Phys. Chem. B* **115**, 14246 (2011).
- [18] G. Moras, A. Klemenz, T. Reichenbach, A. Gola, H. Uetsuka, M. Moseler, and L. Pastewka, Shear melting of silicon and diamond and the disappearance of the polyamorphic transition under shear, *Phys. Rev. Mater.* **2**, 083601 (2018).
- [19] V. L. Deringer, N. Bernstein, G. Csányi, C. Ben Mahmoud, M. Ceriotti, M. Wilson, D. A. Drabold, and S. R. Elliott, Origins of structural and electronic transitions in disordered silicon, *Nature (London)* **589**, 59 (2021).
- [20] B. Haberl, M. Guthrie, D. Sprouster, J. Williams, and J. Bradby, New insight into pressure-induced phase transitions of amorphous silicon: The role of impurities, *J. Appl. Crystallogr.* **46**, 758 (2013).
- [21] E. G. Ponyatovsky, A thermodynamic approach to  $T$ - $P$  phase diagrams of substances in liquid and amorphous states, *J. Phys.: Condens. Matter* **15**, 6123 (2003).
- [22] P. F. McMillan, Polyamorphic transformations in liquids and glasses, *J. Mater. Chem.* **14**, 1506 (2004).
- [23] V. V. Vasisht, S. Saw, and S. Sastry, Liquid-liquid critical point in supercooled silicon, *Nat. Phys.* **7**, 549 (2011).
- [24] E. Rapoport, Model for melting-curve maxima at high pressure, *J. Chem. Phys.* **46**, 2891 (1967).
- [25] L. I. Aptekar, Phase transitions in noncrystalline germanium and silicon, *Dokl. Akad. Nauk SSSR* **249**, 1099 (1979) [*Sov. Phys. Dokl.* **24**, 993 (1979)].
- [26] T. Morishita, How Does Tetrahedral Structure Grow in Liquid Silicon upon Supercooling? *Phys. Rev. Lett.* **97**, 165502 (2006).
- [27] N. Jakse and A. Pasturel, Liquid-Liquid Phase Transformation in Silicon: Evidence from First-Principles Molecular Dynamics Simulations, *Phys. Rev. Lett.* **99**, 205702 (2007).
- [28] P. Ganesh and M. Widom, Liquid-Liquid Transition in Supercooled Silicon Determined by First-Principles Simulation, *Phys. Rev. Lett.* **102**, 075701 (2009).
- [29] D. Daisenberger, M. Wilson, P. F. McMillan, R. Quesada Cabrera, M. C. Wilding, and D. Machon, High-pressure x-ray scattering and computer simulation studies of density-induced polyamorphism in silicon, *Phys. Rev. B* **75**, 224118 (2007).
- [30] K. K. Pandey, N. Garg, K. V. Shanavas, S. M. Sharma, and S. K. Sikka, Pressure induced crystallization in amorphous silicon, *J. Appl. Phys.* **109**, 113511 (2011).
- [31] D. C. Wallace, *Thermodynamics of Crystals* (Wiley, New York, 1972).
- [32] R. Hill, On the elasticity and stability of perfect crystals at finite strain, *Mathematical Proceedings of the Cambridge Philosophical Society* (Cambridge University, Cambridge, England, 1975), Vol. 77, pp. 225-240.
- [33] J. Wang, J. Li, S. Yip, S. Phillpot, and D. Wolf, Mechanical instabilities of homogeneous crystals, *Phys. Rev. B* **52**, 12627 (1995).
- [34] J. Griebler, L. Frérot, J. A. Oldenstaedt, M. H. Müser, and L. Pastewka, Analytic elastic constants in molecular calculations:

- Finite strain, non-affine displacements, and many-body interatomic potentials, [arXiv.2302.08754](https://arxiv.org/abs/2302.08754).
- [35] D. J. Lacks, Localized Mechanical Instabilities and Structural Transformations in Silica Glass under High Pressure, *Phys. Rev. Lett.* **80**, 5385 (1998).
- [36] D. L. Malandro and D. J. Lacks, Relationships of shear-induced changes in the potential energy landscape to the mechanical properties of ductile glasses, *J. Chem. Phys.* **110**, 4593 (1999).
- [37] C. Maloney and A. Lemaitre, Universal Breakdown of Elasticity at the Onset of Material Failure, *Phys. Rev. Lett.* **93**, 195501 (2004).
- [38] A. Lemaître and C. Maloney, Sum rules for the quasi-static and visco-elastic response of disordered solids at zero temperature, *J. Stat. Phys.* **123**, 415 (2006).
- [39] E. D. Cubuk, R. J. S. Ivancic, S. S. Schoenholz, D. J. Strickland, A. Basu, Z. S. Davidson, J. Fontaine, J. L. Hor, Y.-R. Huang, Y. Jiang, N. C. Keim, K. D. Koshigan, J. A. Lefever, T. Liu, X.-G. Ma, D. J. Magagnosc, E. Morrow, C. P. Ortiz, J. M. Rieser, A. Shavit *et al.*, Structure-property relationships from universal signatures of plasticity in disordered solids, *Science* **358**, 1033 (2017).
- [40] D. Richard, M. Ozawa, S. Patinet, E. Stanifer, B. Shang, S. A. Ridout, B. Xu, G. Zhang, P. K. Morse, J.-L. Barrat, L. Berthier, M. L. Falk, P. Guan, A. J. Liu, K. Martens, S. Sastry, D. Vandembroucq, E. Lerner, and M. L. Manning, Predicting plasticity in disordered solids from structural indicators, *Phys. Rev. Mater.* **4**, 113609 (2020).
- [41] M. L. Falk and J. S. Langer, Dynamics of viscoplastic deformation in amorphous solids, *Phys. Rev. E* **57**, 7192 (1998).
- [42] J. Ding, S. Patinet, M. L. Falk, Y. Cheng, and E. Ma, Soft spots and their structural signature in a metallic glass, *Proc. Natl. Acad. Sci. USA* **111**, 14052 (2014).
- [43] M. J. Demkowicz and A. S. Argon, High-Density Liquidlike Component Facilitates Plastic Flow in a Model Amorphous Silicon System, *Phys. Rev. Lett.* **93**, 025505 (2004).
- [44] M. J. Demkowicz and A. S. Argon, Liquidlike atomic environments act as plasticity carriers in amorphous silicon, *Phys. Rev. B* **72**, 245205 (2005).
- [45] K. Huang, *Introduction to Statistical Physics* (CRC, Boca Raton, FL, 2009).
- [46] K. Maeda and S. Takeuchi, Atomistic process of plastic deformation in a model amorphous metal, *Philos. Mag. A* **44**, 643 (1981).
- [47] C. E. Maloney and A. Lemaitre, Amorphous systems in athermal, quasistatic shear, *Phys. Rev. E* **74**, 016118 (2006).
- [48] T. Kumagai, S. Izumi, S. Hara, and S. Sakai, Development of bond-order potentials that can reproduce the elastic constants and melting point of silicon for classical molecular dynamics simulation, *Comput. Mater. Sci.* **39**, 457 (2007).
- [49] A. P. Bartók, J. Kermode, N. Bernstein, and G. Csányi, Machine Learning a General-Purpose Interatomic Potential for Silicon, *Phys. Rev. X* **8**, 041048 (2018).
- [50] V. L. Deringer, N. Bernstein, A. P. Bartók, M. J. Cliffe, R. N. Kerber, L. E. Marbella, C. P. Grey, S. R. Elliott, and G. Csányi, Realistic atomistic structure of amorphous silicon from machine-learning-driven molecular dynamics, *J. Phys. Chem. Lett.* **9**, 2879 (2018).
- [51] T. Reichenbach, G. Moras, L. Pastewka, and M. Moseler, Solid-Phase Silicon Homoepitaxy via Shear-Induced Amorphization and Recrystallization, *Phys. Rev. Lett.* **127**, 126101 (2021).
- [52] M. Parrinello and A. Rahman, Polymorphic transitions in single crystals: A new molecular dynamics method, *J. Appl. Phys.* **52**, 7182 (1981).
- [53] G. J. Martyna, D. J. Tobias, and M. L. Klein, Constant pressure molecular dynamics algorithms, *J. Chem. Phys.* **101**, 4177 (1994).
- [54] W. Shinoda, M. Shiga, and M. Mikami, Rapid estimation of elastic constants by molecular dynamics simulation under constant stress, *Phys. Rev. B* **69**, 134103 (2004).
- [55] D. J. Lacks, First-Order Amorphous-Amorphous Transformation in Silica, *Phys. Rev. Lett.* **84**, 4629 (2000).
- [56] K. M. S. Garcez and A. Antonelli, Pressure-induced transformations in amorphous silicon: A computational study, *J. Appl. Phys.* **115**, 063504 (2014).
- [57] M. Born and K. Huang, *Dynamical Theory of Crystal Lattices* (Clarendon, Oxford, 1954).
- [58] D. C. Wallace and J. L. Patrick, Stability of crystal lattices, *Phys. Rev.* **137**, A152 (1965).
- [59] F. Birch, Finite elastic strain of cubic crystals, *Phys. Rev.* **71**, 809 (1947).
- [60] F. Birch, Elasticity and constitution of the Earth's interior, *J. Geophys. Res.* **57**, 227 (1952).
- [61] T. H. K. Barron and M. L. Klein, Second-order elastic constants of a solid under stress, *Proc. Phys. Soc.* **85**, 523 (1965).
- [62] D. C. Wallace, Thermoelasticity of stressed materials and comparison of various elastic constants, *Phys. Rev.* **162**, 776 (1967).
- [63] J. F. Lutsko, Generalized expressions for the calculation of elastic constants by computer simulation, *J. Appl. Phys.* **65**, 2991 (1989).
- [64] A. Tanguy, J. P. Wittmer, F. Leonforte, and J.-L. Barrat, Continuum limit of amorphous elastic bodies: A finite-size study of low-frequency harmonic vibrations, *Phys. Rev. B* **66**, 174205 (2002).
- [65] M. Tsamados, A. Tanguy, C. Goldenberg, and J.-L. Barrat, Local elasticity map and plasticity in a model Lennard-Jones glass, *Phys. Rev. E* **80**, 026112 (2009).
- [66] H. Mizuno, S. Mossa, and J.-L. Barrat, Measuring spatial distribution of the local elastic modulus in glasses, *Phys. Rev. E* **87**, 042306 (2013).
- [67] D. Richard, G. Kapteijns, J. A. Giannini, M. L. Manning, and E. Lerner, Simple and Broadly Applicable Definition of Shear Transformation Zones, *Phys. Rev. Lett.* **126**, 015501 (2021).
- [68] J. D. Eshelby, The determination of the elastic field of an ellipsoidal inclusion, and related problems, *Proc. R. Soc. London, Ser. A* **241**, 376 (1957).
- [69] T. Albaret, A. Tanguy, F. Boioli, and D. Rodney, Mapping between atomistic simulations and Eshelby inclusions in the shear deformation of an amorphous silicon model, *Phys. Rev. E* **93**, 053002 (2016).
- [70] P. H. Poole, U. Essmann, F. Sciortino, and H. E. Stanley, Phase diagram for amorphous solid water, *Phys. Rev. E* **48**, 4605 (1993).
- [71] K. H. Smith, E. Shero, A. Chizmeshya, and G. H. Wolf, The equation of state of polyamorphic germania glass: A two-domain description of the viscoelastic response, *J. Chem. Phys.* **102**, 6851 (1995).
- [72] V. V. Brazhkin, A. G. Lyapin, O. V. Stalgorova, E. L. Gromnitskaya, S. V. Popova, and O. B. Tsiok, On the nature of

- amorphous-to-amorphous and crystal-to-amorphous transitions under high pressure, *J. Non-Cryst. Solids* **212**, 49 (1997).
- [73] O. B. Tsiok, V. V. Brazhkin, A. G. Lyapin, and L. G. Khvostantsev, Logarithmic Kinetics of the Amorphous-Amorphous Transformations in SiO<sub>2</sub> and GeO<sub>2</sub> glasses under high pressure, *Phys. Rev. Lett.* **80**, 999 (1998).
- [74] C. Fusco, T. Albaret, and A. Tanguy, Role of local order in the small-scale plasticity of model amorphous materials, *Phys. Rev. E* **82**, 066116 (2010).
- [75] A. Kerrache, N. Mousseau, and L. J. Lewis, Amorphous silicon under mechanical shear deformations: Shear velocity and temperature effects, *Phys. Rev. B* **83**, 134122 (2011).
- [76] F. Bolioli, T. Albaret, and D. Rodney, Shear transformation distribution and activation in glasses at the atomic scale, *Phys. Rev. E* **95**, 033005 (2017).
- [77] M. Ozawa, L. Berthier, G. Biroli, A. Rosso, and G. Tarjus, Random critical point separates brittle and ductile yielding transitions in amorphous materials, *Proc. Natl. Acad. Sci. USA* **115**, 6656 (2018).
- [78] F. Varnik, L. Bocquet, and J.-L. Barrat, A study of the static yield stress in a binary Lennard-Jones glass, *J. Chem. Phys.* **120**, 2788 (2004).
- [79] A. Wisitsorasak and P. G. Wolynes, On the strength of glasses, *Proc. Natl. Acad. Sci. USA* **109**, 16068 (2012).
- [80] P. K. Jaiswal, I. Procaccia, C. Rainone, and M. Singh, Mechanical Yield in Amorphous Solids: A First-Order Phase Transition, *Phys. Rev. Lett.* **116**, 085501 (2016).
- [81] G. Parisi, I. Procaccia, C. Rainone, and M. Singh, Shear bands as manifestation of a criticality in yielding amorphous solids, *Proc. Natl. Acad. Sci. USA* **114**, 5577 (2017).
- [82] R. Jana and L. Pastewka, Correlations of non-affine displacements in metallic glasses through the yield transition, *J. Phys. Mater.* **2**, 045006 (2019).
- [83] S. Plimpton, Fast parallel algorithms for short-range molecular dynamics, *J. Comput. Phys.* **117**, 1 (1995).
- [84] A. P. Thompson, H. M. Aktulga, R. Berger, D. S. Bolintineanu, W. M. Brown, P. S. Crozier, P. J. in't Veld, A. Kohlmeyer, S. G. Moore, T. D. Nguyen, R. Shan, M. J. Stevens, J. Tranchida, C. Trott, and S. J. Plimpton, LAMMPS—a flexible simulation tool for particle-based materials modeling at the atomic, meso, and continuum scales, *Comput. Phys. Commun.* **271**, 108171 (2022).
- [85] A. Hjorth Larsen, J. J. Mortensen, J. Blomqvist, I. E. Castelli, R. Christensen, M. Durak, J. Friis, M. N. Groves, B. Hammer, C. Hargus, E. D. Hermes, P. C. Jennings, P. Bjerre Jensen, J. Kermode, J. R. Kitchin, E. Leonhard Kolsbjerg, J. Kubal, K. Kaasbjerg, S. Lysgaard, J. Bergmann Maronsson *et al.*, The atomic simulation environment—a Python library for working with atoms, *J. Phys.: Condens. Matter* **29**, 273002 (2017).
- [86] <https://github.com/libAtoms/matscipy.git>.
- [87] A. Stukowski, Visualization and analysis of atomistic simulation data with ovito—the open visualization tool, *Modell. Simul. Mater. Sci. Eng.* **18**, 015012 (2010).